

# A General PSTD Method to Solve Quantum Scattering in the Fresnel and Far-Field Regions by A Localized Potential of Arbitrary Form

Kun Chen

<sup>a</sup>*Key Laboratory of Quantum Optics, Department of Aerospace Laser Technology and Systems, Shanghai Institute of Optics and Fine Mechanics, Chinese Academy of Sciences, Shanghai, 201800, China*

---

## Abstract

We present a time domain method to solve quantum scattering by an arbitrary potential of finite range. The scattering wave function in full space can be obtained, including the near field, the mid field (i.e. Fresnel region) and the far field. This is achieved by extending several techniques of FDTD computational electrodynamics into the quantum realm. The total-field/scattered-field scheme naturally incorporates the incidence source condition. The wave function in the internal model, including the interaction region and the close near field, is directly computed through PSTD/FDTD iterations. The quantum version of surface equivalence theorem is proven and links the wave function in the external free space to the PSTD/FDTD solution in the internal model. Parallel implementation of PSTD based on overlapping domain decomposition and FFT on local Fourier-basis is briefly discussed. These building blocks unite into a numerical system that provides a general, robust solver to potential scattering problems. Its accuracy is verified by the established partial wave method, by comparing the predictions of both on the central square potential scattering. Further investigations show the far-field solution is inadequate for simulating Fresnel-region effects.

*Keywords:* quantum scattering, Fresnel region, PSTD, total-field/scattered-field, quantum surface equivalence theorem, near-to-distant-field transformation

---

## 1. Introduction

Scattering is a fundamental methodology of physics to detect the structure of matter and study the interaction between the probing particle and the target. In the scenario of nonrelativistic matter wave incidence, such as thermal or cold neutron beam, the problem falls into the category of quantum potential scattering governed by the Schrödinger equation. Since the establishment of quantum theory, methods solving scattering problems have been zealously pursued. In today's standard textbook, rigorous solution is still restricted to the central potential scattering at the far

---

*Email address:* kunchen@siom.ac.cn, kunchen@alum.mit.edu (Kun Chen)

field limit, where the spherical Bessel functions asymptotically approach sine and cosine functions [1, 2]. By partial wave analysis, a phase shift can be numerically retrieved for each partial wave component, and the total scattering wave function at  $r \rightarrow \infty$  becomes the supposition of all these partial waves. For other forms of potentials, unfortunately there is no general method to calculate the solution in a strict way, even in numerical sense. The scattering wave function may be expressed in an analytically closed form, such as the Lippmann-Schwinger integral equation, but it is hard to convert it into actual numbers for comparison with experiment data. Often, approximate methods, such as the Born approximation, become the choice. Furthermore, all these methods can only give results at the far field. They are incapable of predicting the scattering behavior in the Fresnel region.

The Fresnel region sits between the near field and the far field. Its importance has been realized and explored in the development of a novel imaging methodology based on the quantum correlation of incident fields, often referred to as ghost imaging [3–9]. In this scheme, a spatially incoherent wave, either an X-ray or a matter wave, is split into a reference arm and an object arm. Quantum information is encoded in the correlation between the two wavefronts. In the object arm, the detector is placed in the Fresnel region of the scattered field. Intensity correlations between the signals of the two arms are recorded. As is well known, the far field is subject to diffraction limit, whereas the near field poses special instrumental difficulties in arranging the detector. The transmitted signal collected in the Fresnel region provides an intermediately close, sub-diffraction-limit resolution "see-through" of the internals of the target with relatively easy experimental setup.

The boundary between the Fresnel region and the far field is typically characterized by a length  $D^2/\lambda$ , where  $D$  is the size of interaction zone and  $\lambda$  the probing wavelength. In the case of magnetic neutron scattering, the magnetic induction  $\mathbf{B}$  generally scales as  $r^{-3}$ , so the effective  $D$  will be one order of magnitude larger than the object's magnetic structure.

Apart from the field distance, another difficulty in solving potential scattering is the form of the potential function. A general potential could be non-central, time-dependent, even nonlinear (i.e. depending on the wave function itself), and in the event of magnetic neutron scattering, in a matrix form proportional to the vector product of the Pauli matrices and the magnetic induction  $\sigma \cdot \mathbf{B}$  [10]. A precise solution even in the far field is still out of reach by conventional methods.

Electromagnetic wave scattering and de Broglie wave scattering share many similarities. Both have to tackle the problem of solving time-dependent partial differential equations, with a target setup, a numerical injection of the incident wave, and the goal of finding the response at distant sites. After decades' intense development, the finite-difference time-domain (FDTD) technique and its close variant, the pseudo-spectral time-domain (PSTD) technique, have become the standard solver of the Maxwell equations governing electromagnetic scattering [11]. This is the more suitable choice than other approaches, such as the finite-element method, regarding scattering. The advantages of FDTD/PSTD include its capability of large scale modeling and the ability to handle transient response of pulsed incidence. The last point is especially enlightening when we consider neutron spallation sources.

By drawing close analogy between the two kinds of scatterings, many concepts

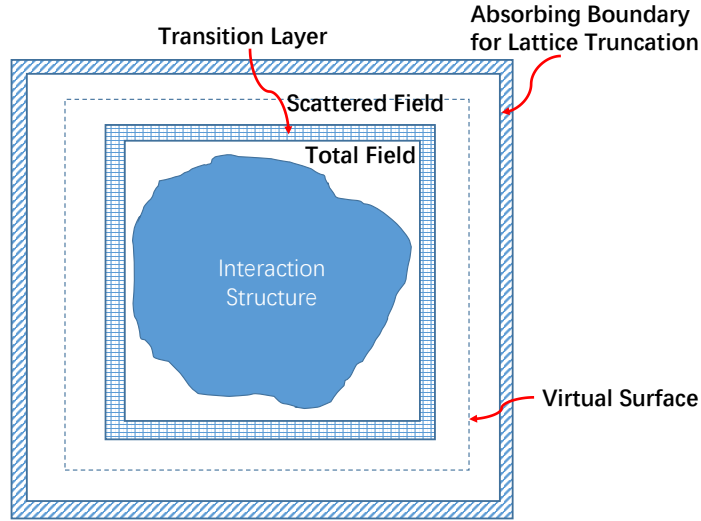


Figure 1: Setup of the Internal Model

from the FDTD/PSTD electrodynamics can be directly extended into the realm of quantum mechanics. Among these are total-field/scattered-field (TF/SF), incident wave source conditions, surface equivalence theorem, virtual surface phasor quantities, and near-to-far-field transformation [11]. So far these ideas have been absent in quantum mechanics. Of course, the mathematical expressions of their quantum version would be distinct from the corresponding electromagnetic version. In the following sections, we will incorporate the above concepts into the Schrödinger equation, derive their theoretical forms from the first principle, develop the FDTD/PSTD numerical algorithms, and combine the various aspects into a modern, general, systematic analyzing technique for quantum potential scattering. The actual coding and large-scale parallel implementation will be focused on Fourier PSTD.

## 2. Internal Model

The incident wave does not vanish at  $\mathbf{r} \rightarrow \infty$ . So the scattering is an unbound state problem of the time-dependent Schrödinger equation (TDSE). This does not mean TDSE has to be solved in infinite space. A careful observation reveals that outside the interaction region, the free propagation of the scattered wave can be separated as an isolated process. Thus TDSE only needs to be solved in a finite space if the interaction is confined to a limited range. Consequently, the entire simulation is divided into two stages. In the first stage, an internal model is constructed (Fig. 1), consisting of only the interaction region, some nearby free space, and a truncation boundary. FDTD/PSTD is applied to the internal model. In the second stage, the scattered wave function outside the internal model is calculated via near-to-distant-field transformation of the first-stage results.

Figure 1 illustrates the general idea of the internal model, bearing resemblance to that of FDTD electrodynamics [11]. Here, the interaction is totally contained in the TF region, whereas the transition layer and the SF region are free space. While the total wave function is employed in the TF, only the pure scattering wave is considered in the SF. The incident wave is handled in the transition layer. The details of Fig. 1 are discussed in the following subsections.

### 2.1. Absorption Boundary Conditions

Discretizing TDSE on finite space requires lattice truncation, otherwise spurious effects will appear at boundaries of an "open" lattice, either as numerical reflections in the finite difference method or as wraparound in the Fourier spectral method. Over the past decades, various numerical techniques have been developed to absorb the outgoing waves and eliminate the reflection from the edges, as if the waves have transparently propagated into the outside infinite space and will never return.

To impose the absorbing boundary condition (ABC), the outer perimeter of the model domain is surrounded by an artificial damping layer of finite width (Fig. 1). The most prominent implementations of the damping include exterior complex scaling (ECS) [12], smooth exterior scaling (SES) [13, 14], perfect matched layer (PML) [15, 16], and complex absorption potential (CAP) [17, 18]. The idea behind ECS and SES is the analytical continuation of the coordinate variable  $x$ . For example, after entering an absorbing boundary from the left,  $x$  is continued to a rising contour into the upper half complex plane, so that the amplitude of the forward propagating wave  $\exp(ikx)$  attenuates along the path. PML introduces a different complex coordinate transformation of variable  $x$ , expressed as

$$x \rightarrow x + e^{i\gamma} \int_{x_0}^x \sigma(\omega) d\omega, \quad (1)$$

where  $\sigma(\omega)$  is a non-negative function, called the absorption profile, and  $\gamma$  is a constant coordinate stretch parameter. Accordingly, the Schrödinger equation undergoes variable change, and extra potential terms appear in the absorbing layer.

However, our numerical experiments on the one dimension free propagation of Gaussian wave, using both FDTD and PSTD, show the above coordinate-transform based ABCs are unstable. In the ECS and SES cases, the wave function quickly blows up near the starting grid of the contour. In the PML case, numerical performance is slightly better, and the wavepacket initially behaves as expected, but eventually blows up after sufficient iterations. Further investigations show these coordinate-transform based ABCs (ECS, SES, PML) all introduce positive imaginary potential near the entry grids into the boundaries. (For example, the two positive spikes of  $Im(V_0)$  in Figure 2 of Ref. [13].) As  $i\hbar\partial\psi/\partial t = H\psi + V_R\psi + iV_I\psi$ , the positive  $V_I$  spikes will cause the wave functions at these grids behave like  $\psi_0 \exp(V_I t)$ . Eventually the exponential growth at these grids will spread to the entire lattice.

On the other hand, a masking multiplication method, introduced in Ref. [17], does render a stable solution. Here, each time iteration comprises two steps. Firstly, the wave function is time-stepped according to the Schrödinger equation,

$$\psi_{(0)}^{n+1} = \psi^{n-1} - i \frac{2\Delta t}{\hbar} H\psi^n, \quad (2)$$

and secondly, the wave function in the absorbing boundary is manually attenuated by multiplying a factor, i.e.,

$$\psi^{n+1} = (1 - \gamma(\mathbf{r})\Delta t) \psi_{(0)}^{n+1}, \quad (3)$$

where

$$\gamma(d) = U_0 / \cosh^2(\alpha d), \quad (4)$$

with  $U_0$  a positive constant,  $\alpha$  the decay factor, and  $d$  the distance from the outmost surface of the absorbing layer. Eq. (3) is equivalent to

$$\frac{\partial \psi}{\partial t} = -\gamma(\mathbf{r})\psi, \quad (5)$$

corresponding to an extra negative imaginary potential (NIP) added to the Hamiltonian. [17]

Eqs. (2)-(3) can be combined and rewritten as

$$\psi^{n+1} = (1 - \gamma\Delta t) \left( \psi^{n-1} - i \frac{2\Delta t}{\hbar} H\psi^n \right), \quad (6)$$

or

$$\psi^{n+1} = e^{-\gamma\Delta t} \left( \psi^{n-1} - i \frac{2\Delta t}{\hbar} H\psi^n \right). \quad (7)$$

Due to the shape of  $\gamma$ ,  $\exp(-\gamma\Delta t)$  serves as a mask. In actual coding, it can be calculated and stored in computer memory before the time-stepping loop starts.

Finally, though the Poshcl-Teller shape of NIP (Eq. (4)) guarantees a stable ABC, this does not preclude other choices of NIP. Especially, the potential can be extended to a complex one with both real and imaginary parts, as far as the imaginary part is kept non-positive. Such design can improve numerical performance [19].

## 2.2. Incident Wave Source Conditions

As discussed in detail in Ref. [11], injecting incident wave source into the computation space lattice is nontrivial. Using hard source, or inserting the incident wave as an initial condition, at each field location in the space lattice will cause profound problems. To overcome the difficulties, a total-field/scattered-field (TF/SF) technique has been developed for plane-wave incidence [11]. In this scheme, the computation lattice is divided into a central core zone (TF) surrounded by an external zone (SF) (Fig. 1). While the TF simulates the detailed wave-structure interaction, the SF concerns purely the scattered wave. The incident wave is absent in both the TF and SF. Its influence only enters the model at the interface between the TF and the SF. Therefore, the incident wave values are only needed at a tiny fraction of the space lattice. This delicate feature not only expedites code execution, but also saves computer memory. Most importantly, it allows simulations on both pulsed and cw wave incidences.

The Maxwell's equations only involve the first-order spatial derivatives, while the Schrödinger equation depends on the second-order ones. This distinction makes the TF/SF formulation of the latter considerably more complicated than the former. In Fig. 1, the TF, the transition layer and the SF are the central framework of the internal model. Within the SF, an imaginary, enclosed virtual surface is set for the purpose of calculating wave function at distant locations outside the internal model. The TF zone should be large enough to contain the effective range of the potential  $V(\mathbf{r})$ . A cutoff of  $r$  should be valid if  $V(\mathbf{r})$  decreases fast enough when  $r$  increases. Consequently,  $V(\mathbf{r})$  is taken as 0 outside the TF. The thickness of the SF should be kept thin, in order to control the size of the internal model and improve code efficiency. Typically two wavelengths should be enough. The virtual surface is configured at the center of the SF.

The TF/SF conversion is based on the fact

$$\psi^{\text{total}}(\mathbf{r}) = \psi^{\text{scat}}(\mathbf{r}) + \psi^{\text{inc}}(\mathbf{r}), \quad (8)$$

with  $\psi^{\text{total}}$ ,  $\psi^{\text{scat}}$ , and  $\psi^{\text{inc}}$  the total, scattered, and incident wave function, respectively. In our numerical model, we intend to use one unique wave function  $\psi(\mathbf{r})$  for the entire computation domain, so that

$$\psi(\mathbf{r}) = \begin{cases} \psi^{\text{total}}(\mathbf{r}) & \mathbf{r} \in \text{TF} \\ \psi^{\text{scat}}(\mathbf{r}) & \mathbf{r} \in \text{SF}. \end{cases} \quad (9)$$

The  $\psi(\mathbf{r})$  within the translation layer will be discussed below.

### 2.2.1. FDTD Version of TF/SF

FDTD solvers of the Maxwell's equations commonly utilize the central finite difference to discretize the first-order spatial derivatives. TF/SF conversion can be achieved on one single layer of grids from each side. On the other hand, the second-order spatial derivatives in the Schrödinger equation require better approximations in order to maintain high numerical accuracy. In FDTD, a good choice is the eighth order central finite difference stencil [15]. For example, in terms of  $y$

$$\frac{\partial^2 \psi}{\partial y^2} \Big|_{i,j,k} = \frac{1}{\Delta y^2} \left[ \alpha_0 \psi|_{i,j,k} + \sum_{\ell=1}^4 \alpha_\ell \left( \psi|_{i,j-\ell,k} + \psi|_{i,j+\ell,k} \right) \right] \quad (10)$$

with the coefficients

$$(\alpha_0, \alpha_1, \alpha_2, \alpha_3, \alpha_4) = \left( -\frac{205}{72}, \frac{8}{5}, -\frac{1}{5}, \frac{8}{315}, -\frac{1}{560} \right). \quad (11)$$

The derivative at the central grid requires 4 grid values to the left and 4 grid values to the right, plus its own value. This complicates the TF/SF conversion for the Schrödinger equation.

Under central finite difference for the time derivative, the wave function in the

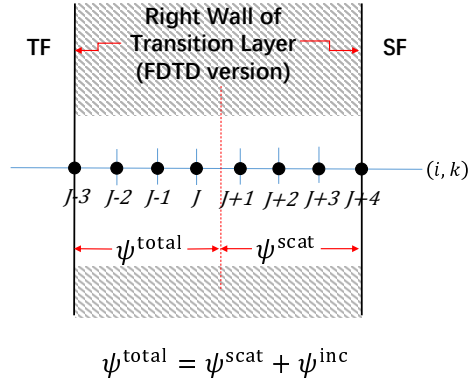


Figure 2: FDTD transition layer and TF/SF conversion. On the four grids left to the center line,  $\psi = \psi^{\text{total}}$ ; on the four grids right to the central line,  $\psi = \psi^{\text{scat}}$ .

TF and the SF share the same updating formula

$$\begin{aligned} \psi_{i,j,k}^{n+1} = & \psi_{i,j,k}^{n-1} - \frac{i2\Delta t}{\hbar} V_{i,j,k} + \frac{i\hbar\Delta t}{m} \left\{ \left( \frac{1}{\Delta x^2} + \frac{1}{\Delta y^2} + \frac{1}{\Delta z^2} \right) \alpha_0 \psi_{i,j,k}^n \right. \\ & + \frac{1}{\Delta x^2} \sum_{\ell=1}^4 \alpha_{\ell} \left( \psi_{i-\ell,j,k}^n + \psi_{i+\ell,j,k}^n \right) + \frac{1}{\Delta y^2} \sum_{\ell=1}^4 \alpha_{\ell} \left( \psi_{i,j-\ell,k}^n + \psi_{i,j+\ell,k}^n \right) \\ & \left. + \frac{1}{\Delta z^2} \sum_{\ell=1}^4 \alpha_{\ell} \left( \psi_{i,j,k-\ell}^n + \psi_{i,j,k+\ell}^n \right) \right\}. \end{aligned} \quad (12)$$

Here, the  $\psi$  is the unique one defined in Eq. (9).

What about the grids in the transition layer? It turns out the transition layer needs to be 8 grid cells thick, 4 at the TF side and 4 at the SF side. Figure 2 illustrates a horizontal  $(ik)$  line across the right wall of the transition layer. Here,  $i$ ,  $j$  and  $k$  denote the indices along the  $x$ ,  $y$  and  $z$  directions, respectively. To avoid complication from the corners, for the time being consider the case where the transverse indices  $i$  and  $k$  are within the TE. Evaluating  $\frac{\partial^2 \psi}{\partial y^2}$  at  $j = J-3, \dots, J$  would now require grid values from the SF side, and vice versa.

However, both sides of Eq. (10) must be kept consistent: the entries must be either all total waves, or all scattered waves. This is where the incident wave comes into play. The consistency condition Eq. (8) serves to convert a scattered wave at the SF side to a total wave,

$$\psi^{\text{total}}|_{i,j,k} = \psi|_{i,j,k} + \psi^{\text{inc}}|_{i,j,k}, \quad j \geq J+1, \quad (13)$$

and oppositely a total wave at the TF side to a scattered wave,

$$\psi^{\text{scat}}|_{i,j,k} = \psi|_{i,j,k} - \psi^{\text{inc}}|_{i,j,k}, \quad j \leq J. \quad (14)$$

This connection naturally inserts the plane wave source into the lattice computation.

Substituting Eqs. (13) and (14) into the Schrödinger equation, we can obtain the updating formula for the transition layer, referred to as the consistency condition. We list the consistency condition for the right wall of transition layer as

$$\psi|_{i,J-3,k}^{n+1} = \left\{ \psi|_{i,J-3,k}^{n+1} \right\}_{\text{Eq. (12)}} + \frac{i\hbar\Delta t}{m\Delta y^2} \alpha_4 \psi^{\text{inc}}|_{i,J+1,k}^n, \quad (15)$$

$$\psi|_{i,J-2,k}^{n+1} = \left\{ \psi|_{i,J-2,k}^{n+1} \right\}_{\text{Eq. (12)}} + \frac{i\hbar\Delta t}{m\Delta y^2} \sum_{\ell=3}^4 \alpha_\ell \psi^{\text{inc}}|_{i,J-2+\ell,k}^n, \quad (16)$$

$$\psi|_{i,J-1,k}^{n+1} = \left\{ \psi|_{i,J-1,k}^{n+1} \right\}_{\text{Eq. (12)}} + \frac{i\hbar\Delta t}{m\Delta y^2} \sum_{\ell=2}^4 \alpha_\ell \psi^{\text{inc}}|_{i,J-1+\ell,k}^n, \quad (17)$$

$$\psi|_{i,J,k}^{n+1} = \left\{ \psi|_{i,J,k}^{n+1} \right\}_{\text{Eq. (12)}} + \frac{i\hbar\Delta t}{m\Delta y^2} \sum_{\ell=1}^4 \alpha_\ell \psi^{\text{inc}}|_{i,J+\ell,k}^n, \quad (18)$$

$$\psi|_{i,J+1,k}^{n+1} = \left\{ \psi|_{i,J+1,k}^{n+1} \right\}_{\text{Eq. (12)}} - \frac{i\hbar\Delta t}{m\Delta y^2} \sum_{\ell=1}^4 \alpha_\ell \psi^{\text{inc}}|_{i,J+1-\ell,k}^n, \quad (19)$$

$$\psi|_{i,J+2,k}^{n+1} = \left\{ \psi|_{i,J+2,k}^{n+1} \right\}_{\text{Eq. (12)}} - \frac{i\hbar\Delta t}{m\Delta y^2} \sum_{\ell=2}^4 \alpha_\ell \psi^{\text{inc}}|_{i,J+2-\ell,k}^n, \quad (20)$$

$$\psi|_{i,J+3,k}^{n+1} = \left\{ \psi|_{i,J+3,k}^{n+1} \right\}_{\text{Eq. (12)}} - \frac{i\hbar\Delta t}{m\Delta y^2} \sum_{\ell=3}^4 \alpha_\ell \psi^{\text{inc}}|_{i,J+3-\ell,k}^n, \quad (21)$$

$$\psi|_{i,J+4,k}^{n+1} = \left\{ \psi|_{i,J+4,k}^{n+1} \right\}_{\text{Eq. (12)}} - \frac{i\hbar\Delta t}{m\Delta y^2} \alpha_4 \psi^{\text{inc}}|_{i,J,k}^n. \quad (22)$$

The first terms on the r.h.s are given by Eq. (12). Derivations for the other five walls are straightforward, and their results are omitted for brevity.

Eqs. (15)-(22) indicate that the grids of the transition layer undergo a two-step updating, one from the lattice, and the other from the incident source. In actual implementation, at each time leapfrog, all grids in the computation domain are firstly updated according to Eq. (12), then the grids of the transition layer are further updated with the incidence source terms, one-by-one for all six walls. It turns out this accumulative updating scheme automatically handles the corners of the transition layer properly, where the walls of different directions overlap.

### 2.2.2. PSTD Version of TF/SF

TF/SF was not available when PSTD was first introduced into computational electromagnetics [20]. The Fourier pseudospectral transform is a global operation. The transform is performed on all grids (in 1D sense, along  $x$ ,  $y$  or  $z$ ). The discontinuity of the field values across the TF/SF interface will excite spurious ripples in the computation lattice, well known as the Gibbs' phenomenon. In addition, the global nature of Fourier transform prevents direct implementation of  $\mathbf{E}^{\text{total}} = \mathbf{E}^{\text{scat}} + \mathbf{E}^{\text{inc}}$  and  $\mathbf{H}^{\text{total}} = \mathbf{H}^{\text{scat}} + \mathbf{H}^{\text{inc}}$ . Another scheme, the pure scattered field formulation becomes an easy choice, in which the Maxwell's equations are reformulated to express the scattered fields as the only unknowns on all grids. However, this approach suffers several drawbacks. Calculations of the incident wave are needed for all grids and at each time step, significantly increasing computation burden. Furthermore,



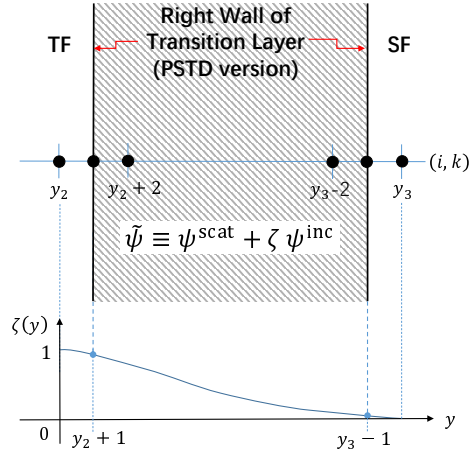


Figure 3: PSTD transition layer and TF/SF conversion

modeling nonlinear structure becomes much harder, as nonlinear effects depend on total fields. This last flaw is especially true to quantum scattering. The potential in a nonlinear Schrödinger equation is itself a function of the total wave functions. The pure scattered field approach is crippled to this kind of simulation.

TF/SF became possible to PSTD when a modified consistency condition was discovered [21]. Adopting the same concept, we can add the incidence source gradually to the scattered wave across the transition layer (Fig. 3), i.e.,

$$\tilde{\psi}(\mathbf{r}, t) \equiv \psi^{\text{scat}}(\mathbf{r}, t) + \zeta(\mathbf{r})\psi^{\text{inc}}(\mathbf{r}, t), \quad (23)$$

where  $\zeta$  is the taper function, with value 0 in the SF and 1 in the TF, and rising smoothly from 0 to 1 across the transition layer. Nicely,  $\tilde{\psi} = \psi^{\text{total}}$  in the TF zone, and  $\tilde{\psi} = \psi^{\text{scat}}$  in the SF zone. Again, a uniq  $\tilde{\psi}$  can be employed in the internal model. Furthermore, the smoothness of  $\zeta$ -function avoids abrupt changes of  $\tilde{\psi}$  and alleviates the Gibbs' oscillation in the PSTD lattice.

An immediate observation is  $(\zeta(\mathbf{r}) - 1)V(\mathbf{r}) = 0$  in the entire computation domain. Another important property is

$$i\hbar \frac{\partial \psi^{\text{inc}}}{\partial t} + \frac{\hbar^2}{2m} \nabla^2 \psi^{\text{inc}} = 0 \quad (24)$$

also in the entire computation domain. Based on these relations, we can obtain

$$i\hbar \frac{\partial \tilde{\psi}}{\partial t} = -\frac{\hbar^2}{2m} \nabla^2 \tilde{\psi} + V(\mathbf{r})\tilde{\psi} + \frac{\hbar^2}{2m} (\nabla^2 \zeta \psi^{\text{inc}} + 2\nabla \zeta \cdot \nabla \psi^{\text{inc}}). \quad (25)$$

The last two terms on the r.h.s originate from the incidence wave. Because  $\nabla^2 \zeta$  and  $\nabla \zeta$  equal to 0 in both the TF zone and the SF zone, these terms only exist in the transition layer.

In 3D,  $\zeta(x, y, z) = \zeta_x(x)\zeta_y(y)\zeta_z(z)$  where the three components share the same function form. For example,

$$\zeta_y(y) = \begin{cases} 0 & y \leq y_0 \\ \xi\left(\frac{y-y_0}{y_1-y_0}\right) & y_0 < y < y_1 \\ 1 & y_1 \leq y \leq y_2 \\ 1 - \xi\left(\frac{y-y_2}{y_3-y_2}\right) & y_2 < y < y_3 \\ 0 & y \geq y_3, \end{cases} \quad (26)$$

where the left transition wall is from  $y_0 + 1$  to  $y_1 - 1$ , the right one from  $y_2 + 1$  to  $y_3 - 1$ . Quenching of the Gibbs' phenomenon depends on a wise choice of the  $\xi$ -function. PSTD electrodynamics takes the integral form of the Blackman-Harris window function (IBH) as the taper function [21]. However, IBH is not analytical and its coefficients are empirical. The precision of IBH is limited to  $10^{-4}$  and in addition, its first derivative is not exactly 0 at  $\rho = 1$ . In the Schrödinger equation, this tiny mismatch can excite Gibbs' oscillation to some extent. For higher precision, we design an optimal taper,

$$\xi(\rho) = \rho - \frac{2}{3\pi} \sin(2\pi\rho) + \frac{1}{12\pi} \sin(4\pi\rho), \quad 0 \leq \rho \leq 1. \quad (27)$$

Note this function is totally analytical. Its curve is close to IBH. Though its values are not strictly between 0 and 1, only the smoothness matters. Its derivatives up to the fourth-order are all exactly 0 at  $\rho = 0$  and  $\rho = 1$ . So the curves  $\zeta_x$ ,  $\zeta_y$  and  $\zeta_z$  are fourth-order smooth.

### 2.2.3. Calculation of the Incident Wave

Fig. 4 illustrates the external surface of the transition layer. The wavefront of an incident plane wave will make initial contact with one of the eight corners. The source distribution in the transition layer is a 1D problem, as the grids sitting on the same wavefront share the same source value. In only a few cases there exist analytical expressions of the incident wave functions, such as the sinusoidal wave and the Gaussian wave packet. For wave packet of arbitrary shape, the 1D Schrödinger equation for the incident wave has to be solved *in free space* concurrently with the 3D Schrödinger equation of scattering at hand. At each time iteration, the 1D source is updated first, deployed to the transition layer, and then the 3D internal model (Fig. 1) updated.

The coordinate origin  $O_{\text{inc}}$  of this 1D axis would be the initial contact point of the incident wave front with the transition layer. Let the unit incident wavevector be

$$\hat{\mathbf{k}}_{\text{inc}} = \hat{\mathbf{x}} \sin\theta \cos\phi + \hat{\mathbf{y}} \sin\theta \sin\phi + \hat{\mathbf{z}} \cos\theta. \quad (28)$$

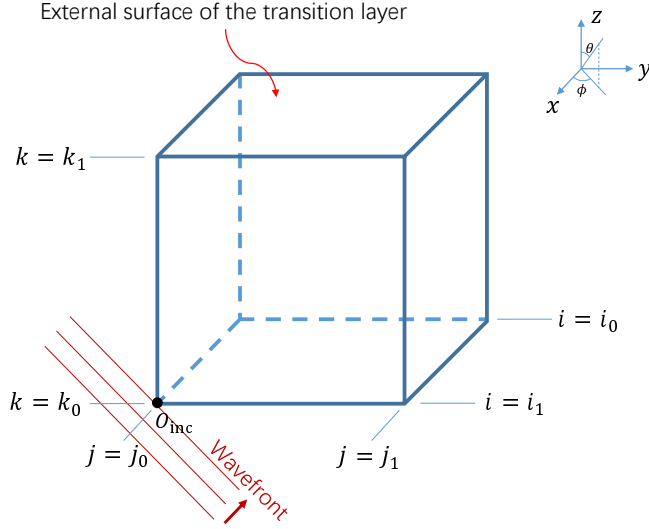


Figure 4: Identification of the origin of the 1D incident wave.

The grid indices  $(O_x, O_y, O_z)$  of the initial contact corner is

$$(O_x, O_y, O_z) = \begin{cases} (i_0, j_0, k_0) & 0^\circ \leq \theta \leq 90^\circ, 0^\circ \leq \phi \leq 90^\circ \\ (i_0, j_1, k_0) & 0^\circ \leq \theta \leq 90^\circ, 90^\circ < \phi \leq 180^\circ \\ (i_1, j_1, k_0) & 0^\circ \leq \theta \leq 90^\circ, 180^\circ < \phi \leq 270^\circ \\ (i_1, j_0, k_0) & 0^\circ \leq \theta \leq 90^\circ, 270^\circ < \phi < 360^\circ \\ (i_0, j_0, k_1) & 90^\circ < \theta \leq 180^\circ, 0^\circ \leq \phi \leq 90^\circ \\ (i_0, j_1, k_1) & 90^\circ < \theta \leq 180^\circ, 90^\circ < \phi \leq 180^\circ \\ (i_1, j_1, k_1) & 90^\circ < \theta \leq 180^\circ, 180^\circ < \phi \leq 270^\circ \\ (i_1, j_0, k_1) & 90^\circ < \theta \leq 180^\circ, 270^\circ < \phi < 360^\circ \end{cases} \quad (29)$$

The coordinate of grid  $(i, j, k)$  on the 1D axis is the projection

$$d = \{(i - O_x)\Delta x \hat{\mathbf{x}} + (j - O_y)\Delta y \hat{\mathbf{y}} + (k - O_z)\Delta z \hat{\mathbf{z}}\} \cdot \hat{\mathbf{k}}_{inc} \quad (30)$$

Generally  $d$  may not fall exactly on a grid on the 1D axis. Wave value on  $d$  is often obtained by nearest neighbor interpolation, or by an inverse FFT method. Note the incidence source terms on the r.h.s. of Eq. (25) also include derivative of the incident wave. So the calculations come in pairs,

$$\psi_{inc}^n|_{i,j,k} = \frac{1}{N} \sum_{\ell=-N/2}^{N/2-1} \mathcal{F}[\psi_{inc}^n]|_{\ell} e^{i \frac{2\pi \ell}{N\Delta} d}, \quad (31)$$

$$(\nabla \psi_{inc}^n)|_{i,j,k} = \frac{\hat{\mathbf{k}}_{inc}}{N} \sum_{\ell=-N/2}^{N/2-1} i \frac{2\pi \ell}{N\Delta} \mathcal{F}[\psi_{inc}^n]|_{\ell} e^{i \frac{2\pi \ell}{N\Delta} d}, \quad (32)$$

with  $N$  the total number of grids along the 1D axis,  $\Delta$  the grid size,  $n$  the time step index, and  $\mathcal{F}$  the 1D FFT operation.

### 2.3. Stability Condition

The choice of time-marching increment  $\Delta t$  is predetermined by the requirement of stability. Though a large  $\Delta t$  makes the simulation take fewer iterations to finish, a runaway result is meaningless. On the other hand, a small  $\Delta t$  increases the computation cost. An optimal  $\Delta t$  should be large enough, and yet keep the total error bounded at any time-step.

The relationship between  $\Delta t$  and the spatial discretization has been studied in the FDTD-Q scheme [22, 23]. In FDTD-Q the real part and imaginary part of the wave function is time-marched alternately to avoid complex numerics. The FDTD-Q stability condition is inapplicable to this work, since complex computation is preferred in order to facilitate the FFT and inverse FFT operations. To derive our version of stability condition, we adopt the approach of Ref. [22]. The discrete form of Schrödinger equation is first separated into a temporal eigenvalue problem and a spatial eigenvalue problem, i.e.

$$i\hbar \frac{\psi^{n+1} - \psi^{n-1}}{2\Delta t} = \lambda_t \psi^n, \quad (33)$$

$$-\frac{\hbar^2}{2m} \nabla^2 \psi(\mathbf{r}, t) + V(\mathbf{r})\psi(\mathbf{r}, t) = \lambda_s \psi(\mathbf{r}, t). \quad (34)$$

A "growth factor"  $q$  is defined to characterize the growth of wave function during the time iteration, i.e.,

$$q = \psi^{n+1}/\psi^n, \quad (35)$$

$$q = \psi^n/\psi^{n-1}. \quad (36)$$

Substituting Eqs. (35)-(36) into Eq. (33) results in an equation for  $q$ ,

$$\frac{1}{2} \left( q - \frac{1}{q} \right) = -i \frac{\lambda_t \Delta t}{\hbar}. \quad (37)$$

Redefine  $q = iQ$  and  $w = -\lambda_t \Delta t / \hbar$ . Eq. (37) is essentially the Joukowski transform

$$w = \frac{1}{2} \left( Q + \frac{1}{Q} \right). \quad (38)$$

The branch cut for the Joukowski transform is the unit circle  $|Q| = 1$ . A  $Q$  within the circle and its reciprocal  $1/Q$  outside the circle will map to the same  $w$  on the complex plane. The transform maps a circle in the  $Q$ -plane to an ellipse in the  $w$ -plane, with the foci at 1 and -1 on the real axis. As  $|Q|$  approaches 1, the ellipse shrinks to the line interval  $[-1, 1]$  on the real axis. On the unit circle,  $Q = e^{i\varphi}$  ( $0 \leq \varphi < 2\pi$ ). There is  $w = \cos \varphi$  and  $-1 \leq w \leq 1$ . The stability requirement imposes condition on  $|q|$ . If  $|q| \rightarrow 0$ ,  $\psi$  vanishes, whereas if  $|q| \rightarrow \infty$ ,  $\psi$  explodes. Neither is stable. When  $|q|$  ( $= |Q|$ ) is around 1, small  $\Delta t$  brings small change in  $\psi$ . In this case the mapped  $w$  is in the vicinity of the interval line discussed above. Thus, we have the condition for  $\lambda_t$

$$|Re(w)| = \left| Re \left( \frac{\lambda_t \Delta t}{\hbar} \right) \right| \leq 1. \quad (39)$$

### 2.3.1. FDTD

To process Eq. (34), the most general solution can be considered as a superposition of plane waves. For each plane wave component, the 8th-order central finite difference (Eqs. (10)-(11)) is applied to Eq. (34) with  $\psi(\mathbf{r}, t) = \exp[i(k_x x + k_y y + k_z z - \omega t)]$ . A calculation gives

$$\lambda_s = \frac{\hbar^2}{2m} \left[ \frac{1}{\Delta_x^2} f(k_x \Delta_x) + \frac{1}{\Delta_y^2} f(k_y \Delta_y) + \frac{1}{\Delta_z^2} f(k_z \Delta_z) \right] + V, \quad (40)$$

$$f(\delta) = \frac{16}{35} \sin^8 \frac{\delta}{2} + \frac{32}{45} \sin^6 \frac{\delta}{2} + \frac{4}{3} \sin^4 \frac{\delta}{2} + 4 \sin^2 \frac{\delta}{2}. \quad (41)$$

Because consistency requires  $\lambda_t = \lambda_s$ , Eq. (39) is linked to Eq. (40). If the maximum value  $|Re(w)|_{max} \leq 1$ , Eq. (39) is guaranteed. This leads to the sufficient (but not the necessary) stability condition for the eighth-order central FDTD

$$\Delta t \leq \frac{\hbar}{\frac{1024\hbar^2}{315m} \left[ \frac{1}{\Delta x^2} + \frac{1}{\Delta y^2} + \frac{1}{\Delta z^2} \right] + |V|_{max}}. \quad (42)$$

### 2.3.2. PSTD

The plane wave supposition argument is unnecessary for PSTD. In FFT language, Eq. (34) converts to

$$\lambda_s \psi = -\frac{\hbar^2}{2m} \left\{ \mathcal{F}_x^{-1} [-k_x^2 \mathcal{F}_x[\psi]] + \mathcal{F}_y^{-1} [-k_y^2 \mathcal{F}_y[\psi]] + \mathcal{F}_z^{-1} [-k_z^2 \mathcal{F}_z[\psi]] \right\} + V \psi, \quad (43)$$

where  $\mathcal{F}_x$  and  $\mathcal{F}_x^{-1}$  denote the 1D FFT and inverse FFT over the  $x$  direction, and so on. One important property of PSTD is that the kinetic energy representable by the discrete lattice has an upper bound. The maximum  $ks$  on the r.h.s of Eq. (43) are  $\pm\pi/\Delta x$ ,  $\pm\pi/\Delta y$  and  $\pm\pi/\Delta z$  respectively. Any larger  $k$  will be aliased to a value within the limits. Therefore,

$$\lambda_s < \frac{\hbar^2 \pi^2}{2m} \left( \frac{1}{\Delta x^2} + \frac{1}{\Delta y^2} + \frac{1}{\Delta z^2} \right) + |V|_{max}. \quad (44)$$

Again, the consistency requirement  $\lambda_t = \lambda_s$  and the condition  $|Re(w)|_{max} \leq 1$  lead to the sufficient (but not the necessary) stability condition of PSTD

$$\Delta t \leq \frac{\hbar}{\frac{\hbar^2 \pi^2}{2m} \left[ \frac{1}{\Delta x^2} + \frac{1}{\Delta y^2} + \frac{1}{\Delta z^2} \right] + |V|_{max}}. \quad (45)$$

Comparing Eq. (45) with Eq. (42), we notice that the *critical time step*, the maximum time increment which maintains the stability, for PSTD is smaller than that for FDTD.

## 2.4. PSTD: Elimination of Numerical Phase Velocity Error For Monochromatic Wave

Deviation of the phase velocity of numerical wave from the true physical velocity arises when the spatial and time coordinates are discretized. For FDTD on a rectangular grid lattice, a numerical wave would propagate faster along the diagonal of

a grid cell than along the three edges. This anisotropy is absent in PSTD, because the spatial derivatives are converted into strict spectral operations without resort to finite difference approximations. On the other hand, the finite time-step  $\Delta t$  still affects the velocity. For a monochromatic wave  $\psi = \exp(i\mathbf{k} \cdot \mathbf{x} - iEt/\hbar)$ , the PSTD Schrödinger equation is

$$-\frac{\hbar^2}{2m} \left\{ \mathcal{F}_x^{-1} [-k_x^2 \mathcal{F}_x [\psi]] + \mathcal{F}_y^{-1} [-k_y^2 \mathcal{F}_y [\psi]] + \mathcal{F}_z^{-1} [-k_z^2 \mathcal{F}_z [\psi]] \right\} = i\hbar \frac{\partial \psi}{\partial t}. \quad (46)$$

Here,  $k_x^2$ ,  $k_y^2$ , and  $k_z^2$  are fixed values, and can be taken out of the inverse FFTs. Applying the central finite difference approximation to the time derivative, we have

$$k^2 = \frac{2mE}{\hbar^2} \operatorname{sinc} \left( \frac{E\Delta t}{\hbar} \right). \quad (47)$$

At the limit  $\Delta t \rightarrow 0$ , Eq. (47) reduces to the physical formula  $\hbar^2 k^2 = 2mE$ . The time discretization distorted the relation by a factor  $\eta = \operatorname{sinc}(E\Delta t/\hbar)$ . If we rescale the kinetic energy term by factor  $\eta$ , i.e.  $-\frac{\hbar^2}{2m} \nabla^2 \rightarrow -\eta \frac{\hbar^2}{2m} \nabla^2$ , this numerical artifact will completely disappear. Thus, for monochromatic wave incidence, the phase velocity discrepancy can be perfectly corrected. Furthermore, impulsive wave incidence has potentially a broad spectrum. The numerical dispersion of phase velocity is cancelled at the central wavelength and largely reduced at the side wings.

### 2.5. PSTD Updating Formula

A careful examination of Eq. (25) reveals that it can be converted to a dimensionless form. Assuming the central wavelength of the incident wave is  $\lambda_0$ . Correspondingly other central parameters are: central wavevector  $k_0 = 2\pi/\lambda_0$ , central energy  $E_0 = \hbar^2 k_0^2/2m$ , central reduced wavelength  $\lambda_0 = \lambda_0/2\pi$ , and central angular frequency  $\omega_0 = E_0/\hbar$ . Define the dimensionless time and spatial variables as

$$\tau \equiv \omega_0 t, \quad \bar{x} \equiv x/\lambda_0, \quad \bar{y} \equiv y/\lambda_0, \quad \bar{z} \equiv z/\lambda_0. \quad (48)$$

Thus one period of time and space are both  $2\pi$ . The expression of Eq. (25) is now simplified to

$$\frac{\partial \tilde{\psi}}{\partial \tau} = i\eta \bar{\nabla}^2 \tilde{\psi} - i \frac{V}{E_0} \tilde{\psi} - i [\bar{\nabla}^2 \zeta \psi_{\text{inc}} + 2\bar{\nabla} \zeta \cdot \bar{\nabla} \psi_{\text{inc}}]. \quad (49)$$

Here, the symbol  $\bar{\nabla}$  denotes spatial gradient over  $\bar{x}$ ,  $\bar{y}$  and  $\bar{z}$ . Further, the stability condition Eq. (45) becomes

$$\Delta \tau \leq \left[ \pi^2 \left( \frac{1}{\Delta \bar{x}^2} + \frac{1}{\Delta \bar{y}^2} + \frac{1}{\Delta \bar{z}^2} \right) + \frac{|V|_{\max}}{E_0} \right]^{-1}. \quad (50)$$

We use Eq. (7) to impose the ABC. In 3D three independent  $\gamma$  functions (Eq. (4)),  $\gamma(\bar{x})$ ,  $\gamma(\bar{y})$  and  $\gamma(\bar{z})$  are set for the  $x$ ,  $y$  and  $z$  directions. The ABC multiplier

$$\Gamma(\bar{x}, \bar{y}, \bar{z}) = e^{-\gamma(\bar{x})\Delta \tau} e^{-\gamma(\bar{y})\Delta \tau} e^{-\gamma(\bar{z})\Delta \tau} \quad (51)$$

can be prepared beforehand and stored in computer memory. The PSTD updating formula for Eq. (49) is then

$$\begin{aligned} \tilde{\psi}|_{i,j,k}^{n+1} = & \Gamma_{i,j,k} \left\{ \tilde{\psi}|_{i,j,k}^{n-1} - 2i\eta\Delta\tau \left( \mathcal{F}_{\bar{x}}^{-1} \left[ \bar{k}_{\bar{x}}^2 \mathcal{F}_{\bar{x}} \left[ \tilde{\psi}^n \right] \right] \right. \right. \\ & \left. \left. + \mathcal{F}_{\bar{y}}^{-1} \left[ \bar{k}_{\bar{y}}^2 \mathcal{F}_{\bar{y}} \left[ \tilde{\psi}^n \right] \right] + \mathcal{F}_{\bar{z}}^{-1} \left[ \bar{k}_{\bar{z}}^2 \mathcal{F}_{\bar{z}} \left[ \tilde{\psi}^n \right] \right] \right) \right|_{i,j,k} \\ & \left. - 2i\Delta\tau \frac{V_{i,j,k}}{E_0} \tilde{\psi}|_{i,j,k}^n - 2i\Delta\tau \left[ \bar{\nabla}^2 \zeta \psi_{\text{inc}}^n + 2\bar{\nabla} \zeta \cdot \bar{\nabla} \psi_{\text{inc}}^n \right] \right|_{i,j,k} \left. \right\}. \quad (52) \end{aligned}$$

Note almost all FFT software libraries shift the index for  $k$  to  $0, \dots, N-1$ . In Eq. (52), when calculating the factor  $\bar{k}^2$  within the  $\mathcal{F}^{-1}$ , the index must be shifted back to the range  $-N/2, \dots, N/2-1$ .

In the special case of sinusoidal wave incidence, the last term on the r.h.s. of Eq. (52) can be factorized to a product of phasor component and a time exponent  $\exp(-in\Delta\tau)$ . There is no need to solve a 1D incidence source equation. The phasor component can be calculated beforehand and stored in computer memory. Calculation of the time exponent has one further simplification. Factors  $\sin\Delta\tau$  and  $\cos\Delta\tau$  can be calculated beforehand and stored in computer memory. Since  $\sin(n+1)\Delta\tau = \sin n\Delta\tau \cos\Delta\tau + \cos n\Delta\tau \sin\Delta\tau$  and  $\cos(n+1)\Delta\tau = \cos n\Delta\tau \cos\Delta\tau - \sin n\Delta\tau \sin\Delta\tau$ , the sine and cosine of  $(n+1)\Delta\tau$  can be obtained by four multiplications and two additions, where  $\sin n\Delta\tau$  and  $\cos n\Delta\tau$  is calculated in time step  $n$ , stored in computer memory, recursively used in time step  $n+1$ , and so on. This starts at  $n=1$ . Thus the costly series call to sin and cos functions are avoided.

## 2.6. Parallel Implementation of PSTD

Traditional FFT is a global operation involving all data points across the entire computation domain. Modern supercomputers are often distributed-memory cluster systems interconnected via ultra-fast networks. Data exchange between processing units is through message-passing interface (MPI). The particular difficulty of PSTD on global basis is the misalignment of FFT and the subsequent inverse FFT on the same node. Two massive global data transpositions are required for each time step, through non-blocking MPI all-to-all data exchange between all possible node-to-node pairs. The mutual MPI calls can dramatically slow down the code running. Because CPU speeds are orders of magnitude faster than that of networking units, a high efficiency simulation should promote the percentage of in-node computation and lower the percentage of inter-node communications. The FFT on local-Fourier-basis eliminates the requirement for all-to-all data exchanges, while retaining the accuracy of the global FFT [24, 25]. This approach contains several ingredients:

- Overlapping domain decomposition to divided the computation domain into sub-domains in the  $x$ -,  $y$ -, and  $z$ -directions. Each sub-domain has halo regions on all six domain walls. Data in the halos are first copied from the corresponding grids of its neighbor nodes, and then weighted by smoothing factors. Thus, the amount of data exchange is cut-down to the halo grids.

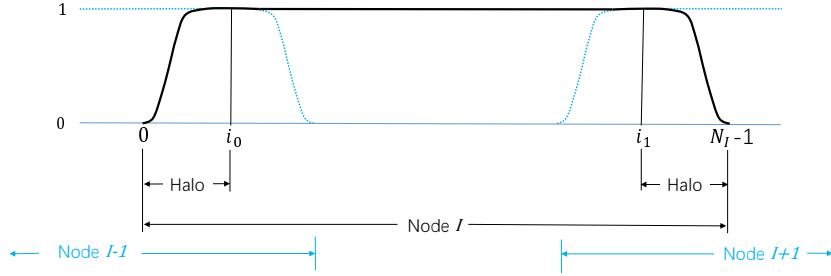


Figure 5: The overlapping between adjacent subdomains and the halo regions.

- Only after a certain distance into the halo, the weighting factors starts to taper the remaining tail of the halo down to zero. This leaves the immediate neighboring grids unchanged and preserves the derivatives on the core grids. In the meantime the FFT on local data evades wraparound effect.
- The FFT and its inverse are performed on local data only, as shown in Fig. 5. The  $N_I$  local grid data consists of the left halo  $0, \dots, i_0 - 1$ , the right halo  $i_1 + 1, \dots, N_I - 1$ , and the internal core grids  $i_0, \dots, i_1$ . Only the core grids are updated at each time-marching. Going to 3D, the  $N_{\bar{x}}$ ,  $N_{\bar{y}}$  and  $N_{\bar{z}}$  in Eq. (52) are then the number of grids in the local sub-domain.

In our implementation, Eq. (27) also serves as the smooth tapering function. Let  $n_t$  be the number of grids for tapering. We require the halo width  $n_{\text{halo}}$  be at least  $n_t + 4 + 1$ . This guarantees at least 4 proximal grids with unchanged data and makes the derivatives more accurate than the 8th-order central finite difference stencil.  $n_t$  is a number to control the steepness of tapering. The extra one is reserved for holding 0 to overcome FFT wraparound. Then the thickness for data exchange is  $n_t + 4$ . Now the weighting factors are given as

$$w[l] = \xi \left( \frac{l}{n_t + 1} \right), \quad l = 1, \dots, n_t. \quad (53)$$

The index  $i$  is counted longitudinally from distal to proximal, and only  $n_t$  layers of grids are weighted.

### 3. Near-to-Distant-Field Transformation

To both the Maxwell equations and the Schrödinger equation, it is challenging to obtain numerical solutions in infinite domain from finite domain computations. Scattering problems utilize the solutions at remote detection sites, in either the Fresnel region or the far field. It would be unwise to create lattice to cover the entire space from the interaction region all the way to the detection point. The vast grid number makes this problem intractable, costly and impractical. FDTD/PSTD solvers of the Maxwell equations employ the near-to-far-field transformation (NTFF), a direct outcome of the surface equivalence theorem of electromagnetic



fields, to obtain far-field solution [11]. In NTFE, an imaginary virtual box enclosing the entire interaction region is set. By the surface equivalence theorem, the original interaction structure can be replaced by the surface currents on the box *with the inside structure totally nulled out*. The surface currents come from the direct FDTD/PSTD computations in the internal model, and field values outside the box become surface integrals of these currents with the Green's function. Integrals on merely the six surfaces of the box significantly relieve the computation burden. Below, we derive the quantum version of the theorem, and identify the surface terms required for the integral. Because the Fresnel region is also concerned, the word near-to-distant-field (NTDF) is more appropriate than NTFE. Furthermore, in order to maintain numerical accuracy in the Fresnel region, a semi-analytical approach is designed to conduct the surface integrals.

### 3.1. Surface Equivalence Theorem

Similar to the derivation of the surface equivalence theorem for electromagnetic fields[26], an enclosed surface  $S$  is first defined to completely surround the interaction area of the Schrödinger potential. This implies the potential has finite range. If the potential is unbounded in range, a range cutoff is valid if the potential drops rapidly as  $r$  increases.

Let the volume bounded by  $S$  be  $V$ . A step function is defined on  $V$ :

$$P(\mathbf{r}) = \begin{cases} 0 & \text{if } \mathbf{r} \in V, \\ 1 & \text{if } \mathbf{r} \notin V. \end{cases} \quad (54)$$

Note this definition is opposite to Ref. [26] because our goal is the solution outside  $V$ . The derivative of a step function equals the delta function, so the gradient of  $P(\mathbf{r})$  would be nontrivial only at the interface  $S$ , but 0 elsewhere. We can symbolically write

$$\nabla P(\mathbf{r}) = \mathbf{n}(\mathbf{r}) \delta_S(\mathbf{r}) \quad (55)$$

where  $\mathbf{n}$  is the outward surface normal of  $V$ . Any volume integral involving the surface delta function  $\delta_S(\mathbf{r})$  would reduce to a surface integral over  $S$ .

Consider the time-independent Schrödinger equation and its Green's function, i.e.,

$$-\frac{\hbar^2}{2m} \nabla^2 \Psi(\mathbf{r}) + V(\mathbf{r}) \Psi(\mathbf{r}) = E \Psi(\mathbf{r}), \quad (56)$$

$$\nabla^2 G(\mathbf{r}|\mathbf{r}_0) + k^2 G(\mathbf{r}|\mathbf{r}_0) = \delta(\mathbf{r} - \mathbf{r}_0) \quad (57)$$

with  $E$  the energy of the incident plane wave,  $\mathbf{k}$  the wave vector, and  $k = \sqrt{2mE}/\hbar$ . Define a new wave function

$$\Psi_{\text{DF}}(\mathbf{r}) \equiv P(\mathbf{r}) \Psi(\mathbf{r}). \quad (58)$$

Here,  $\Psi_{\text{DF}}$  is identical to  $\Psi$  in the distant field, but vanishes inside  $V$ . In addition, the potential term  $P(\mathbf{r})V(\mathbf{r}) = 0$ . This leads to the following,

$$\nabla^2 \Psi_{\text{DF}}(\mathbf{r}) + k^2 \Psi_{\text{DF}}(\mathbf{r}) = (\nabla^2 P(\mathbf{r}) + 2\nabla P(\mathbf{r}) \cdot \nabla) \Psi(\mathbf{r}). \quad (59)$$

As both  $\nabla^2 P$  and  $\nabla P$  are non-zero only on  $S$ , the r.h.s of Eq. (59) serves as the surface source for  $\psi_{\text{DF}}$ . All the internal details of  $V(\mathbf{r})$  do not explicitly appear in Eq. (59). However,  $V(\mathbf{r})$  implicitly determines the distant field wave  $\Psi_{\text{DF}}$  through the near-field waves on  $S$ , i.e.  $\Psi$  and  $\nabla\Psi$ , which are solved in the internal model.

A straightforward calculation presents

$$\Psi_{\text{DF}}(\mathbf{r}) = \iint_S d\mathbf{s}' \cdot [G(\mathbf{r}'|\mathbf{r}) \nabla' \Psi(\mathbf{r}') - \nabla' G(\mathbf{r}'|\mathbf{r}) \Psi(\mathbf{r}')], \quad (60)$$

where  $d\mathbf{s}'$  is the surface element of outward unit normal. Using the Green's function expression

$$G(\mathbf{r}'|\mathbf{r}) = -\frac{e^{ik|\mathbf{r}'-\mathbf{r}|}}{|\mathbf{r}'-\mathbf{r}|}, \quad (61)$$

Eq. (60) is further simplified to

$$\Psi_{\text{DF}}(\mathbf{r}) = -\frac{1}{4\pi} \iint_S d\mathbf{s}' \cdot \left[ \nabla' \Psi(\mathbf{r}') + \left( -ik + \frac{1}{|\mathbf{r}'-\mathbf{r}|} \right) \frac{\mathbf{r}'-\mathbf{r}}{|\mathbf{r}'-\mathbf{r}|} \Psi(\mathbf{r}') \right] \frac{e^{ik|\mathbf{r}'-\mathbf{r}|}}{|\mathbf{r}'-\mathbf{r}|}. \quad (62)$$

So far in the derivation, the  $\Psi$  in Eq. (60) are the total wave function. Recall that the virtual surfaces are located in free space. For scattering problems, the incident plane wave  $\psi^{\text{inc}}$  is a solution to the Schrödinger equation in infinite free space. By setting the potential  $V(\mathbf{r}) = 0$ , as a special case of the above proof,  $\psi^{\text{inc}}$  independently satisfies Eq. (60). Since  $\Psi^{\text{total}} = \Psi^{\text{scat}} + \psi^{\text{inc}}$ , the scattered wave function  $\Psi^{\text{scat}}$  also obeys Eq. (60).

The surface equivalence theorem (Eq. (60)) makes processing quantum scattering of arbitrary potential possible, whenever the potential goes to 0 fast enough as the distance  $r$  increases. This only requirement on potential over  $r$  is the same as the conventional partial-wave method on central potentials. There is no other restrictions on the detailed form of  $V(\mathbf{r})$  or on the specific shape of  $S$ . Therefore, scattering by a central or non-central potential, of scalar form or vector-dependent, or spin-magnetic-field interactions can all be solved. In practice,  $S$  is often arranged as a virtual rectangular box in the near field region of the scattered field. Thus, the integral of Eq. (62) simplifies to integration on its six surfaces, and the gradient operation  $\nabla'$  on each surface becomes one single derivate, for example, on  $x$  for the front/back surfaces. Finally, Eq. (62) identifies the surface terms required for the NTDF transformation be the  $\Psi$  and  $\nabla\Psi$  on the six virtual surfaces.

However, in actual modeling, surface terms on slightly larger planes are stored, in order to facilitate the 2D-FFT described in the next section. In Fig. 6, the shaded box represents the virtual enclosure of size  $L_x^v \times L_y^v \times L_z^v$ . Its surfaces are referred to as the virtual surfaces. Each virtual surface sits on a virtual plane, which is a body cross section of the internal model. During the FDTD/PSTD time iterations, it is the  $\Psi$  and  $\nabla\Psi$  on the six virtual planes that will be accumulated and stored. Due to the absorbing boundary (Fig. 1),  $\Psi$  and  $\nabla\Psi$  decay to 0 at the edges. Therefore, the 2D-FFT on the virtual planes (not the virtual surfaces) can automatically avoid the wrap-around effect.

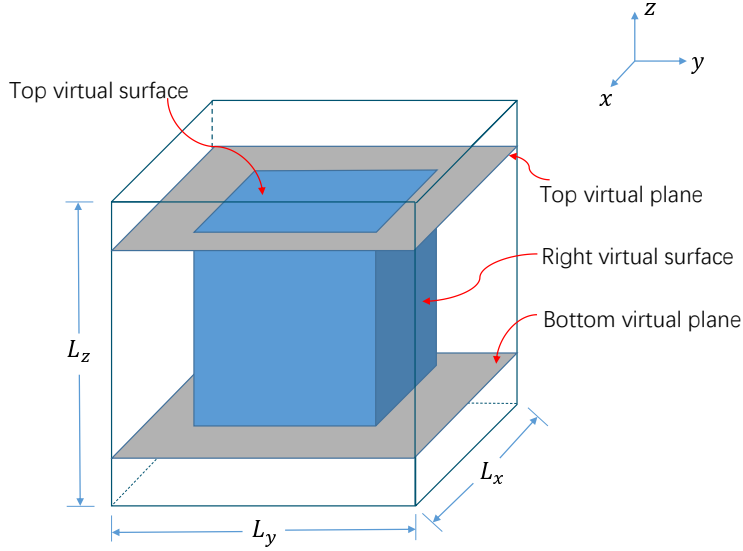


Figure 6: The virtual surface is part of the virtual plane which is a cross section of the internal model (Fig. 1.)

### 3.2. Semi-Analytical Integration for NTDF

FDTD electrodynamics applies a far-field approximation to simplify the surface integral, i.e.,

$$\frac{e^{ik|\mathbf{r}-\mathbf{r}'|}}{|\mathbf{r}-\mathbf{r}'|} \approx \frac{e^{ikr}}{r} e^{-ikr' \cos \Phi} \quad (63)$$

where  $\mathbf{r}$  is the far field location,  $\mathbf{r}'$  the surface grid, and  $\Phi$  the angle between  $\mathbf{r}$  and  $\mathbf{r}'$ . Assume the virtual box size is  $L$ . The far field condition  $kL^2 \ll r$  is violated in the Fresnel region, rendering the phase expansion invalid. In addition, the denominator on the l.h.s of Eq. (63)  $|\mathbf{r}-\mathbf{r}'|$  also significantly deviates from  $r$ . Fortunately, the FDTD/PSTD grids are typically of subwavelength size. The Fresnel field does satisfy the far-field condition of each surface cell. The denominator  $|\mathbf{r}-\mathbf{r}'|$  can be replaced with the distance between the field coordinate and the cell center, and thus will be different for different cells. The overall surface integral (Eq. (62)) can then be disassembled into summations of the integrals on each individual cells.

A mathematical technique can further improve the numerical accuracy of the integration, especially useful for PSTD, since PSTD typically sets coarser grids than FDTD. To reformat a discrete function into an analytical expression, first we conduct FFT on the discrete data, then we use the results as the coefficients for the inverse Fourier transform. Without losing generality, we describe the procedure on

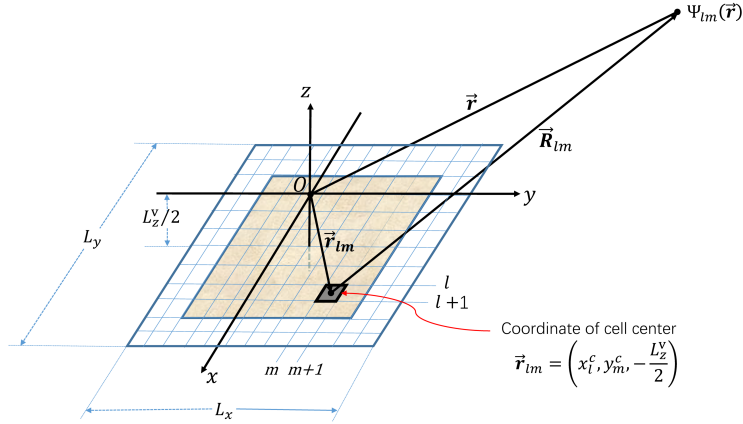


Figure 7: An illustration of the integration on a cell  $(l, m)$  at the bottom virtual surface.

the bottom surface,

$$\begin{aligned} \psi_{\text{an}}^{\text{b}}(x, y) &= \frac{1}{N_x N_y} \sum_{i'=-N_x/2}^{N_x/2-1} \sum_{j'=-N_y/2}^{N_y/2-1} \mathcal{F}_{xy} [\psi^{\text{b}}] \Big|_{i'j'} \\ &\quad \exp \left[ i \frac{2\pi i'}{N_x \Delta x} \left( x + \frac{L_x}{2} \right) + i \frac{2\pi j'}{N_y \Delta y} \left( y + \frac{L_y}{2} \right) \right], \end{aligned} \quad (64)$$

where  $\mathcal{F}_{xy}$  is the 2D-FFT on the discrete  $\psi^{\text{b}}$ ,  $L_x$  and  $L_y$  are the size of the bottom virtual plane (Fig. 7). Expression for  $\partial\psi^{\text{b}}/\partial z$  is similar.

Eq. (64) allows the integral on a surface cell to be carried out semi-analytically. Figure 7 illustrates cell  $(l, m)$  on the bottom virtual surface. Let  $x_l^c = (x_l + x_{l+1})/2$ ,  $y_m^c = (y_m + y_{m+1})/2$ . The coordinate of the cell center is  $\mathbf{r}_{lm} = (x_l^c, y_m^c, -L_z^v/2)$ ,  $\mathbf{R}_{lm} = \mathbf{r} - \mathbf{r}_{lm}$ , and unit vector  $\hat{\mathbf{R}}_{lm} = \mathbf{R}_{lm}/R_{lm}$ . Within this cell, an off-cell-center location  $\mathbf{r}'$  satisfies  $\mathbf{r} - \mathbf{r}' = \mathbf{R}_{lm} - (\mathbf{r}' - \mathbf{r}_{lm})$ , where  $\delta\mathbf{r}' = \mathbf{r}' - \mathbf{r}_{lm}$  is the local offset from the center and coplanar with the cell surface. Because  $\Delta x$  and  $\Delta y$  are subwavelength size, the Fresnel region always satisfies  $(\Delta x)^2 \ll \lambda R$ . The Green's function (Eq. (61)) can now be approximated as  $-\frac{e^{ikR_{lm}}}{R_{lm}} e^{-ik\hat{\mathbf{R}}_{lm} \cdot \delta\mathbf{r}'}$ . Consequently, the contribution from bottom surface cell  $(l, m)$  to the wave function at  $\mathbf{r}$  is

$$\begin{aligned} \Psi_{lm}^{\text{b}}(\mathbf{r}) &= \frac{\Delta x \Delta y e^{ikR_{lm}}}{4\pi N_x N_y R_{lm}} \sum_{i'=-N_x/2}^{N_x/2-1} \sum_{j'=-N_y/2}^{N_y/2-1} (-1)^{i'+j'} e^{2\pi i \left( i' \frac{x_l^c}{L_x} + j' \frac{y_m^c}{L_y} \right)} \\ &\quad \left\{ \mathcal{F}_{xy} \left[ \frac{\partial\psi}{\partial z} \right] \Big|_{i'j'} + \left( ik - \frac{1}{R_{lm}} \right) \hat{\mathbf{R}}_{lm} \cdot \hat{\mathbf{z}} \mathcal{F}_{xy} [\psi] \Big|_{i'j'} \right\} \\ &\quad \text{sinc} \left( \pi \frac{i'}{N_x} - \frac{k\Delta x}{2} \hat{\mathbf{R}}_{lm} \cdot \hat{\mathbf{x}} \right) \text{sinc} \left( \pi \frac{j'}{N_y} - \frac{k\Delta y}{2} \hat{\mathbf{R}}_{lm} \cdot \hat{\mathbf{y}} \right). \end{aligned} \quad (65)$$

On the r.h.s of the above equation, we have suppressed the "bottom" superscript to the  $\psi$  for clarity. Similarly, the contribution from the top surface cell at  $\mathbf{r}_{lm} =$

$(x_l^c, y_m^c, L_z^v/2)$  is

$$\begin{aligned} \Psi_{lm}^t(\mathbf{r}) &= -\frac{\Delta x \Delta y e^{ikR_{lm}}}{4\pi N_x N_y R_{lm}} \sum_{i'=-N_x/2}^{N_x/2-1} \sum_{j'=-N_y/2}^{N_y/2-1} (-1)^{i'+j'} e^{2\pi i \left( i' \frac{x_l^c}{L_x} + j' \frac{y_m^c}{L_y} \right)} \\ &\quad \left\{ \mathcal{F}_{xy} \left[ \frac{\partial \psi}{\partial z} \right] \Big|_{i'j'} + \left( ik - \frac{1}{R_{lm}} \right) \hat{\mathbf{R}}_{lm} \cdot \hat{\mathbf{z}} \mathcal{F}_{xy} [\psi] \Big|_{i'j'} \right\} \\ &\quad \text{sinc} \left( \pi \frac{i'}{N_x} - \frac{k\Delta x}{2} \hat{\mathbf{R}}_{lm} \cdot \hat{\mathbf{x}} \right) \text{sinc} \left( \pi \frac{j'}{N_y} - \frac{k\Delta y}{2} \hat{\mathbf{R}}_{lm} \cdot \hat{\mathbf{y}} \right). \end{aligned} \quad (66)$$

For a back/front surface cell,

$$\begin{aligned} \Psi_{mn}^{k/f}(\mathbf{r}) &= \pm \frac{\Delta y \Delta z e^{ikR_{mn}}}{4\pi N_y N_z R_{mn}} \sum_{j'=-N_y/2}^{N_y/2-1} \sum_{k'=-N_z/2}^{N_z/2-1} (-1)^{j'+k'} e^{2\pi i \left( j' \frac{y_m^c}{L_y} + k' \frac{z_n^c}{L_z} \right)} \\ &\quad \left\{ \mathcal{F}_{yz} \left[ \frac{\partial \psi}{\partial x} \right] \Big|_{j'k'} + \left( ik - \frac{1}{R_{mn}} \right) \hat{\mathbf{R}}_{mn} \cdot \hat{\mathbf{x}} \mathcal{F}_{yz} [\psi] \Big|_{j'k'} \right\} \\ &\quad \text{sinc} \left( \pi \frac{j'}{N_y} - \frac{k\Delta y}{2} \hat{\mathbf{R}}_{mn} \cdot \hat{\mathbf{y}} \right) \text{sinc} \left( \pi \frac{k'}{N_z} - \frac{k\Delta z}{2} \hat{\mathbf{R}}_{mn} \cdot \hat{\mathbf{z}} \right) \end{aligned} \quad (67)$$

with  $+/-$  for the back/front surfaces, respectively. The definitions of  $R_{mn}$ ,  $y_m^c$  and  $z_n^c$  are similar to the bottom surface.

For a left/right surface cell, we have

$$\begin{aligned} \Psi_{ln}^{l/r}(\mathbf{r}) &= \pm \frac{\Delta x \Delta z e^{ikR_{ln}}}{4\pi N_x N_z R_{ln}} \sum_{i'=-N_x/2}^{N_x/2-1} \sum_{k'=-N_z/2}^{N_z/2-1} (-1)^{i'+k'} e^{2\pi i \left( i' \frac{x_l^c}{L_x} + k' \frac{z_n^c}{L_z} \right)} \\ &\quad \left\{ \mathcal{F}_{xz} \left[ \frac{\partial \psi}{\partial y} \right] \Big|_{i'k'} + \left( ik - \frac{1}{R_{ln}} \right) \hat{\mathbf{R}}_{ln} \cdot \hat{\mathbf{y}} \mathcal{F}_{xz} [\psi] \Big|_{i'k'} \right\} \\ &\quad \text{sinc} \left( \pi \frac{i'}{N_x} - \frac{k\Delta x}{2} \hat{\mathbf{R}}_{ln} \cdot \hat{\mathbf{x}} \right) \text{sinc} \left( \pi \frac{k'}{N_z} - \frac{k\Delta z}{2} \hat{\mathbf{R}}_{ln} \cdot \hat{\mathbf{z}} \right) \end{aligned} \quad (68)$$

with  $+/-$  for the left/right surfaces, respectively.

Finally, the scattered wave function at the distant location  $\mathbf{r}$  is

$$\Psi(\mathbf{r}) = \sum_{l,m} \left[ \Psi_{lm}^b(\mathbf{r}) + \Psi_{lm}^t(\mathbf{r}) \right] + \sum_{m,n} \left[ \Psi_{mn}^k(\mathbf{r}) + \Psi_{mn}^f(\mathbf{r}) \right] + \sum_{l,n} \left[ \Psi_{ln}^l(\mathbf{r}) + \Psi_{ln}^r(\mathbf{r}) \right]. \quad (69)$$

The summation indices  $l$ ,  $m$  and  $n$  are within the virtual surfaces.

### 3.3. Extracting Virtual Surface Data from Time-Domain Computations

The inputs to the r.h.s of Eqs. (65)-(68) are all time-independent. These are actually the phasors of the time-dependent wave function and its derivatives. On the other hand, the outputs of FDTD/PSTD internal model calculations are time-marching values. Section 8.3 of Ref. [11] prescribes a procedure to extract phasor quantities from time-varying fields. During an FDTD/PSTD run, a recursive discrete temporal Fourier transform is applied to the virtual surface fields "on the fly" for

each frequency of interest. Such algorithm also works unchanged in the Schrödinger situation, i.e.

$$\check{\psi}|_{lm} = \sum_n \psi|_{lm}^n e^{i\omega n\Delta t}, \quad (70)$$

$$(\nabla\check{\psi})|_{lm} = \sum_n (\nabla\psi)|_{lm}^n e^{i\omega n\Delta t}, \quad (71)$$

$$\check{\psi}^{\text{inc}}|_{O_x O_y O_z} = \sum_n \psi^{\text{inc}}|_{O_x O_y O_z}^n e^{i\omega n\Delta t}. \quad (72)$$

Note the angular frequency  $\omega$  actually means  $\omega_1, \omega_2, \dots$  for broadband incidence. Eqs. (70)-(72) are repeated for each frequency independently. Here,  $(O_x, O_y, O_z)$  is the 1D origin where the incident wave makes initial contact with the transition layer (Eq. (29)). The stored phasor values which will be directly used in Eqs. (65)-(68) are the scaled ones,

$$\psi|_{lm} = \frac{\check{\psi}|_{lm}}{\check{\psi}^{\text{inc}}|_{O_x O_y O_z}}, \quad (73)$$

$$(\nabla\psi)|_{lm} = \frac{(\nabla\check{\psi})|_{lm}}{\check{\psi}^{\text{inc}}|_{O_x O_y O_z}}. \quad (74)$$

This algorithm allows an impulsive wideband incident wave source condition. The response of the scattering system at multi-wavelengths can be obtained in one run. In comparison, a monochromatic sinusoidal wave source only provides the response at one wavelength. Multi-wavelength response will require multiple runs, once for each wavelength.

For the case of sinusoidal wave incidence, we need to wait enough cycles for the numerical results becoming steady. Afterwards we start the temporal Fourier transform (Eqs. (70)-(72)) and continue the simulation for one more cycle to accumulate the virtual surface phasor data.

For the case of pulsed incidence, the phasor accumulation starts at the first time iteration and continues to the end.

### 3.4. Validation of NTDF

In order to test the accuracy of the NTDF transformation, we consider a spherical wave originated from the center of a virtual box, generate the required virtual surface data, input the data into Eqs. (64)-(69), and check whether we can recover the spherical wave function in the near field, the mid field (i.e., the Fresnel region), and the far field.

In a parallel computing environment of two nodes, the internal model space is decomposed into two subdomains, forming a  $1 \times 2 \times 1$  topology. A lattice of  $384 \times 192 \times 384$  grids is built on each subdomain. The overlapping halo is 15 grids thick. The spherical wave function  $\exp(i\bar{r})/\bar{r}$  with  $\bar{r} = kr$  is used as the golden standard. The grid size is  $\Delta\bar{x} = \Delta\bar{y} = \Delta\bar{z} = \pi/10$ , corresponding to 20 grids per wavelength along the three axis directions. The virtual surfaces are the six planes  $\bar{x}_{\pm} = \pm 41.3119$ ,  $\bar{y}_{\pm} = \pm 36.5996$ , and  $\bar{z}_{\pm} = \pm 41.3119$ . The distance from the origin to the diagonal corners is 68.9411. This labels the near end of the external field. The far field condition,

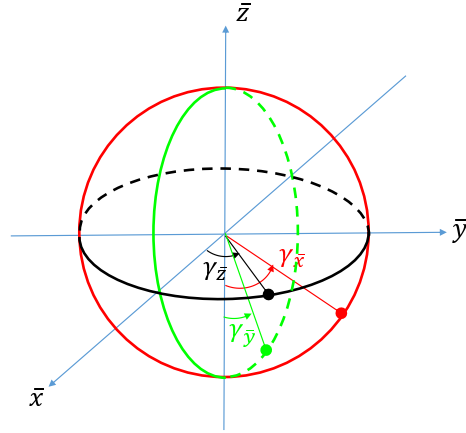


Figure 8: Definition of the Euler angle  $\gamma$

$\bar{r}_{\text{threshold}} \sim (\bar{x}_+ - \bar{x}_-)^2 / \lambda \approx 6800$ , characterizes the boundary between the Fresnel region and the far field.

The surface terms of the spherical wave on the six virtual surfaces are analytically generated. The wave functions on three characteristic planes (Fig. 8), the  $x - y$ ,  $y - z$ , and  $x - z$  planes, are accordingly reconstructed. The coordinate of the wave function is best described by the Euler angles  $(\alpha, \beta, \gamma)$  of the scattering plane ( $y$ -convention) [1]. The first two Euler angle values  $(\alpha, \beta)$  are:  $x - y$  plane,  $(0^\circ, 0^\circ)$ ;  $y - z$  plane,  $(0^\circ, 90^\circ)$ ;  $x - z$  plane,  $(90^\circ, 90^\circ)$ . The definition of the Euler angle  $\gamma$  is given in Fig. 8. Three radii,  $\bar{r} = 100, 2000, 10000$ , are selected, representing the near, mid, and far fields, respectively. A spherical wave should be only a function of  $\bar{r}$  and exhibit no dependence on the three Euler angles. In deed, the NTDF transformed wave functions in Fig. 9 show excellent agreement with the original analytical spherical wave at all external fields. Furthermore, because the fields within the virtual surfaces have been obtained by the direct FDTD/PSTD calculation, our technique can solve the quantum potential scattering in the full 3D space.

#### 4. PSTD Validation Using the Scattering by Central Square Potentials

A golden standard is required in order to validate our numerical algorithm. Among existing scattering techniques, only the partial wave method on spherically symmetric potential can provide relative rigorous numerical solutions *in the far field* after careful cutoffs of  $l$  and the potential range  $r$  [27]. Other kind of methods or other forms of potentials would need to resort to some kind of approximations. The partial wave method, the decomposition of wave function into summations of  $(l, m)$  components, and the expression of the scattering cross-section in terms of the phase shifts  $\delta_l$  are the standard context of quantum mechanics textbooks [1, 2]. Details in numerically seeking  $\delta_l$ s are also well described [27].

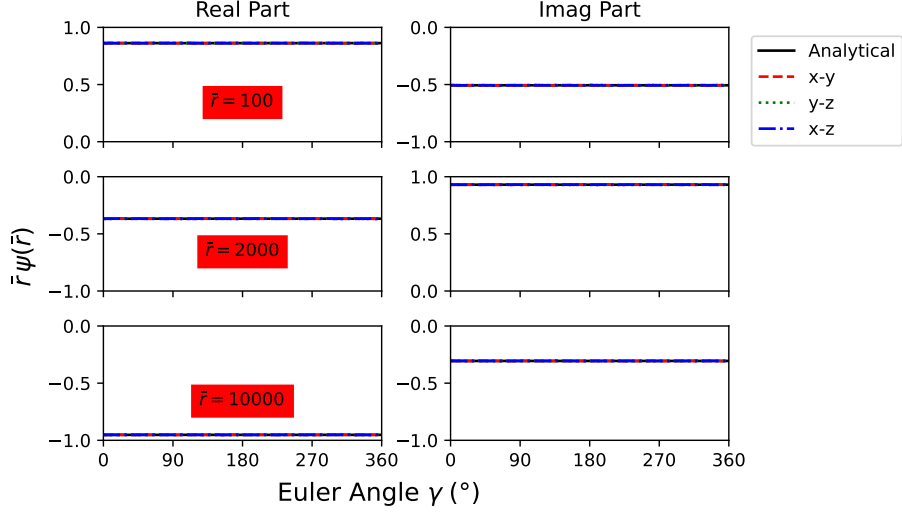


Figure 9: The reconstructed vs. the analytical spherical wave functions along the circles on the  $x-y$ ,  $y-z$ ,  $x-z$  planes (Fig. 8 at three different radii).

The central square potential for testing is given as

$$V(\bar{r}) = \begin{cases} sE_0 & \bar{r} \leq 4\pi \\ 0 & \bar{r} > 4\pi \end{cases} \quad (75)$$

with  $E_0$  the energy of the incident sinusoidal plane wave,  $\bar{r}(= r/\lambda_0)$  the reduced radius, and  $s$  a scaling factor. If  $s < 0$ , it is a potential well, and vice versa. The potential's amplitude and width are both characterized using the parameters of the incident wave. In Fig. 10a four central square potentials are set up, with  $s = 1, 0.5, -0.5, -1$ , respectively. The radius is  $4\pi$ , corresponding to two incident wavelengths. The partial wave solutions of the far-field differential cross-sections are given in Fig. 10b. Because the incident direction is along the  $y$ -axis, in the  $x-y$  and  $y-z$  scattering planes, the Euler angle  $\gamma = 90^\circ$  corresponds to the zero scattering angle.

The four potentials in Fig. 10a are plugged into our PSTD algorithm. The size of the scatterer is  $8\pi$ , so the threshold for the far field would be  $\bar{r}_{\text{th}} \approx 64\pi^2$ . The setup for the modeling is as follows. An overlapping domain decomposition of  $1 \times 2 \times 1$  topology is configured on a two-node parallel platform. A lattice of  $288 \times 160 \times 288$  grids is established on each subdomain, with  $\Delta\bar{x} = \Delta\bar{y} = \Delta\bar{z} = \pi/10$ , corresponding to 20 grids per wavelength. The time increment is  $\Delta\tau = \pi/1000$ , per the requirement of Eq. (50). The widths of the ABC, the SF, the transition layer, and the overlapping halo are 40, 41, 12, and 15 grids, respectively. The parameters for Eq. (4) are  $U_0 = 5.0$  and  $\alpha = 0.1/\text{grid}$ . The virtual surfaces are set on the six middle planes of the SF. The sinusoidal incident wave is along the  $y$ -axis.

Figure 11 presents our far field solutions to the scattering cross-sections at  $\bar{r} = 2 \times 10^4$ , together with the partial wave solutions in Fig. 11. Clearly, the PSTD curves and the partial wave predictions coincide in all cases.



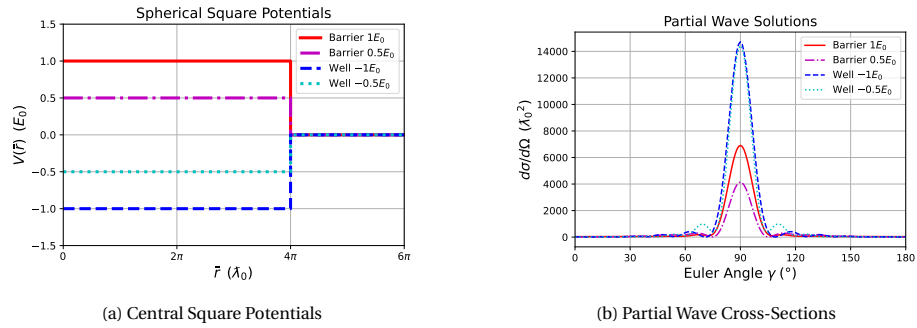


Figure 10: The partial wave solutions of four central square potentials.

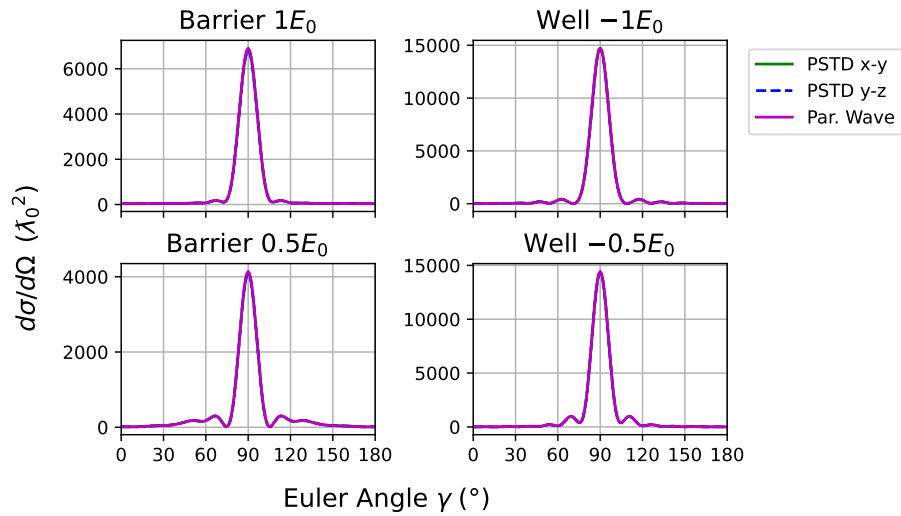


Figure 11: The differential cross-sections calculated using our algorithm at  $\bar{r} = 20000$  vs. the predictions by the partial wave method.

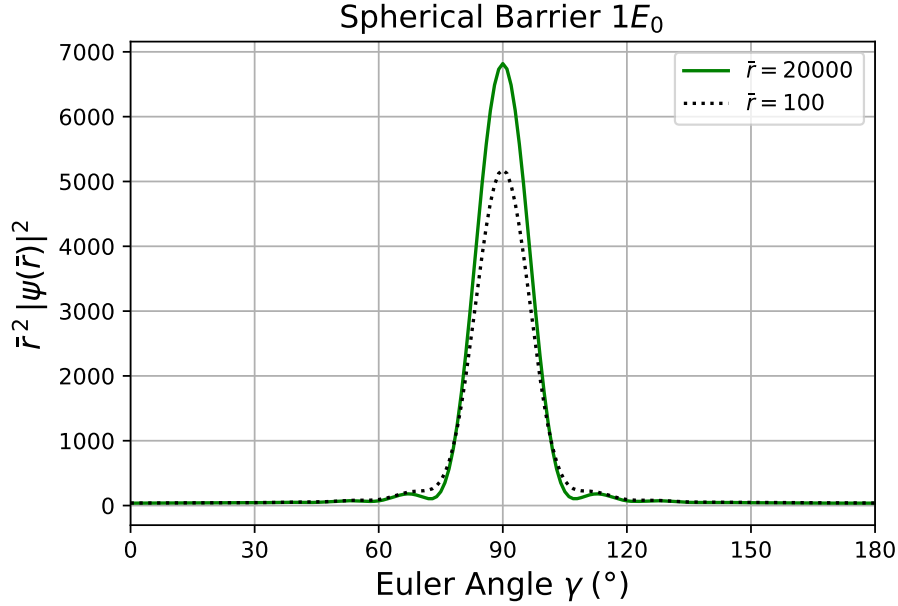


Figure 12: The Fresnel region vs. the far field.

In the far field, the scatterer's size is viewed like a point, and thus the outgoing scattering wave is reduced to a spherical wave. However, in the near field and the Fresnel region, the scatterer's size is nontrivial. Set  $\bar{r} = 100$ , a distance in the Fresnel region, and acquire the wave function. Figure 12 shows significant difference between the Fresnel region and the far field.

## 5. Conclusion

In this work, we have developed a highly accurate numerical technique to solve the problem of quantum potential scattering, by drawing analogy to the mature techniques of computational electrodynamics. The wave function in the interaction zone (i.e. the internal field) and the close near field is directly solved by the FDTD/PSTD computations. The surface terms on a virtual enclosing box are obtained. The wave function in the free space outside the box is calculated through the integration over these surfaces, derived from the surface equivalence theorem. The total-field/scattered-field scheme efficiently and accurately introduces the incident wave into the model. The TF enables the processing of various potentials. Except for the requirement of finite force range, there is no other limit to the interaction forms, allowing non-central forces, time-variant potentials, and nonlinear effects.

To validate the surface equivalence theorem, a spherical wave was precisely reconstructed using NTDF, in regions from the near field, to the mid field (i.e. Fresnel region), and to the far field. The entire algorithm was tested on four central square

potentials. The numerical results show perfect agreement with the partial wave predictions. Further, a significant difference was demonstrated between the Fresnel region and the far field, indicating future simulation using Fresnel-region detection cannot employ far-field results. Immediately, the capability of processing arbitrary potential scattering in the Fresnel region makes simulations on magnetic neutron ghost imaging possible. This work may see other potential applications in studies of atomic and nuclear scatterings.

### Acknowledgements

This work was supported by the National Natural Science Foundation of China under Grant Project No. 12075305.

### References

- [1] J. J. Sakurai, J. Napolitano, *Modern Quantum Mechanics*, Second Edition, Pearson Education, Inc., San Francisco, CA, 2011.
- [2] C. Cohen-Tannoudji, B. Diu, F. Laloë, *Quantum Mechanics*, Vol. 2, Wiley, New York, 2005.
- [3] H. Yu, R. Lu, S. Han, H. Xie, G. Du, T. Xiao, D. Zhu, Fourier-transform ghost imaging with hard x rays, *Phys. Rev. Lett.* 117 (2016) 113901.
- [4] D. Pelliccia, A. Rack, M. Scheel, V. Cantelli, D. M. Paganin, Experimental x-ray ghost imaging, *Phys. Rev. Lett.* 117 (2016) 113902.
- [5] R. I. Khakimov, B. M. Henson, D. K. Shin, S. S. Hodgman, R. G. Dall, K. G. H. Baldwin, A. G. Truscott, Ghost imaging with atoms, *Nature* 540 (2016) 100.
- [6] S. Li, F. Cropp, K. Kabra, T. J. Lane, G. Wetzstein, P. Musumeci, D. Ratner, Electron ghost imaging, *Phys. Rev. Lett.* 121 (2018) 114801.
- [7] K. Chen, S. Han, Microscopy for atomic and magnetic structures based on thermal neutron Fourier-transform ghost imaging, *ArXiv e-prints* (2018). [arXiv: 1801.10046](https://arxiv.org/abs/1801.10046).
- [8] A. M. Kingston, G. R. Myers, D. Pelliccia, F. Salvemini, J. J. Bevitt, U. Garbe, D. M. Paganin, Neutron ghost imaging, *Physical Review A* 101 (2020) 053844.
- [9] S. S. Hodgman, W. Bu, S. B. Mann, R. I. Khakimov, A. G. Truscott, Higher-order quantum ghost imaging with ultracold atoms, *Phys. Rev. Lett.* 122 (2019) 233601.
- [10] G. L. Squires, *Introduction to the Theory of Thermal Neutron Scattering*, Dover Publications, Mineola, New York, 1996.
- [11] A. Taflove, S. C. Hagness, *Computational Electrodynamics, The Finite-Difference Time-Domain Method*, Third Edition, Artech House, Norwood, MA, 2005.

- [12] C. W. McCurdy, D. A. Horner, T. N. Rescigno, Time-dependent approach to collisional ionization using exterior complex scaling, *Phys. Rev. A* 65 (2002) 042714.
- [13] N. Moiseyev, Derivations of universal exact complex absorption potentials by the generalized complex coordinate method, *J. Phys. B: At. Mol. Opt. Phys.* 31 (1998) 1431.
- [14] U. V. Riss, H.-D. Meyer, The transformative complex absorbing potential method: a bridge between complex absorbing potentials and smooth exterior scaling, *J. Phys. B: At. Mol. Opt. Phys.* 31 (1998) 2279.
- [15] A. Nissen, H. O. Karlsson, G. Kreiss, A perfectly matched layer applied to a reactive scattering problem, *J. Chem. Phys.* 133 (2010) 054306.
- [16] A. Nissen, G. Kreiss, An optimized perfectly matched layer for the Schrödinger equation, *Commun. Comput. Phys.* 9 (2011) 147.
- [17] R. Kosloff, D. Kosloff, Absorbing boundaries for wave propagation problems, *J. Comput. Phys.* 63 (1986) 363.
- [18] A. A. Silaev, A. A. Romanov, N. V. Vvedenskii, Multi-hump potentials for efficient wave absorption in the numerical solution of the time-dependent Schrödinger equation, *J. Phys. B: At. Mol. Opt. Phys.* 51 (2018) 065005.
- [19] J. Y. Ge, J. Z. H. Zhang, Use of negative complex potential as absorbing potential, *J. Chem. Phys.* 108 (1998) 1429.
- [20] Q. H. Liu, The PSTD algorithm: A time-domain method requiring only two cells per wavelength, *Microw. Opt. Techn. Lett.* 15 (1997) 158.
- [21] X. Gao, M. S. Mirotznik, D. W. Prather, A method for introducing soft sources in the PSTD algorithm, *IEEE Trans. Antennas Propaga.* 52 (2004) 1665.
- [22] A. Soriano, E. A. Navarro, J. A. Porti, V. Such, Analysis of the finite difference time domain technique to solve the Schrödinger equation for quantum devices, *J. Appl. Phys.* 95 (2004) 8011.
- [23] W. Dai, G. Li, R. Nassar, S. Su, On the stability of the FDTD method for solving a time-dependent Schrödinger equation, *Numer. Methods Partial Differ. Equ.* 21 (2005) 1140.
- [24] M. Israeli, L. Vozovoi, A. Averbuch, Spectral multidomain technique with local Fourier basis, *J. Sci. Comput.* 8 (1993) 135.
- [25] M. Ding, K. Chen, Staggered-grid PSTD on local Fourier basis and its applications to surface tissue modeling, *Opt. Express* 18 (2010) 9236.
- [26] I. V. Lindell, Huygen's principle in electromagnetics, *IEE Proc.-Sci. Meas. Technol.* 143 (1996) 103.
- [27] J. M. Thijssen, *Computational Physics, Second Edition*, Cambridge University Press, Cambridge, UK, 2007.